Journal of Power Sources 195 (2010) 1829–1840

Contents lists available at ScienceDirect

Journal of Power Sources

journal homepage: www.elsevier.com/locate/jpowsour

Effect of composition of ($La_{0.8}Sr_{0.2}MnO_3$–Y_2O_3-stabilized ZrO_2) cathodes: Correlating three-dimensional microstructure and polarization resistance

James R. Wilson[a], J. Scott Cronin[a], Anh T. Duong[b], Sherri Rukes[a], Hsun-Yi Chen[c], Katsuyo Thornton[c], Daniel R. Mumm[b], Scott Barnett[a,*]

[a] Department of Materials Science and Engineering, Northwestern University, 2220 Campus Drive, Evanston, IL 60208, USA
[b] Department of Chemical Engineering and Materials Science, 916 Engineering Tower, University of California-Irvine, Irvine, CA 92697, USA
[c] Department of Materials Science and Engineering, University of Michigan, 2300 Hayward Street, Ann Arbor, MI 48109, USA

ARTICLE INFO

Article history:
Received 31 August 2009
Received in revised form
23 September 2009
Accepted 30 September 2009
Available online 9 October 2009

Keywords:
Solid oxide fuel cells
Three-dimensional (3D) microstructure
Focused ion beam (FIB) tomography
Cathodes

ABSTRACT

Composite $La_{0.8}Sr_{0.2}MnO_3$ (LSM)–Y_2O_3-stabilized ZrO_2 (YSZ) cathodes with compositions ranging from 30:70 to 70:30 wt.% LSM:YSZ were studied both electrochemically and microstructurally. Polarization resistance was lowest for the 50 wt.% YSZ composition, and increased symmetrically as the composition deviated from this value. Serial-sectioning using focused ion beam-scanning electron microscopy was implemented to reconstruct the three-dimensional cathode microstructure. Various averaged structural parameters were determined versus composition, including phase volume fractions, surface area densities, total triple-phase boundary (TPB) densities, interfacial curvatures, phase tortuosities, and the levels of phase connectivity. Typically >90% of the pore and YSZ networks were found to be intra-connected to the surrounding phase, but the LSM networks showed lower connected fractions, as low as 37.5% for a LSM weight fraction of 30%. The composition dependences of the total TPB density and electrochemically-active TPB density (*i.e.*, TPB's on three fully intra-connected phases) were shown to agree reasonably well with simple "sphere-packing" structural models. An electrochemical model that accounted for the linear-specific resistance of TPB's, phase intra-connectivity, and oxygen ion transport in the YSZ as influenced by its tortuosity, was found to provide reasonable agreement with the measured polarization resistance versus composition.

1. Introduction

The most common cathode in state of the art solid oxide fuel cells (SOFCs) utilizes a mixture of $La_{1-x}Sr_xMnO_3$ (LSM) and 8 mol% Y_2O_3-stabilized ZrO_2 (YSZ) [1–5]. LSM–YSZ composites have played an important role in the development of SOFC technology by providing relatively low cathode polarization resistance, R_P, at reduced ($\leq$800 °C) operating temperature [1,4,6–8]. The cathode performance is determined in part by the properties of LSM and YSZ, but it is also strongly dependent on the microstructure. In particular, R_P for LSM-based cathodes is usually associated with three-phase boundaries (TPB's), sites where the electrochemical oxygen reduction can readily occur [9]. TPB's are lines where all three phases are in contact, and hence the TPB density is a measure of the *inter*-connectivity of the microstructure. It has also been shown that *intra*-connectivity (*i.e.*, percolation), the availability of continuous network pathways within each phase, is also important since the species involved in the oxygen reduction reaction – electrons in LSM, oxygen ions in YSZ, and oxygen molecules in pores – must be able to reach TPB's [9–11]. TPB's can be electrochemically active only when this criterion is satisfied. Thus, an ideal electrode structure maximizes both its inter- and intra-connectivities. Similarly, the tortuosity of pathways within each phase can also impact transport to and from TPB's [10,11].

Most of the LSM–YSZ studies have focused on cathodes with ~50 vol% YSZ. Qualitatively, this composition is a reasonable choice because it helps to assure good intra-connectivity of the solid phases. However, relatively few experimental studies have reported the variation of R_P with LSM–YSZ composition, or ascertained the structural factors that produce a low R_P at a given composition. Haanappel et al. [12] reported a highest SOFC power density at a weight ratio of 50:50 LSM:YSZ, while Zhao et al. [9] reported a maximum power density at an LSM–YSZ composition of ~60 vol% YSZ. An optimal composition of 50 vol% GDC was reported for LSM–GDC cathodes [13]. Recent composite electrode structural models predict that the composition expected to yield the lowest R_P, *i.e.*, where the density of electrochemically-active TPB's is highest, can vary from at least 40–60 vol% YSZ depending on the LSM and YSZ particle sizes [14]. Further study of the effect of LSM–YSZ composition is warranted not only to find the optimal composition for

* Corresponding author. Tel.: +1 847 491 2447; fax: +1 847 491 7820.
E-mail address: s-barnett@northwestern.edu (S. Barnett).

0378-7753/$ – see front matter © 2009 Elsevier B.V. All rights reserved.
doi:10.1016/j.jpowsour.2009.09.074

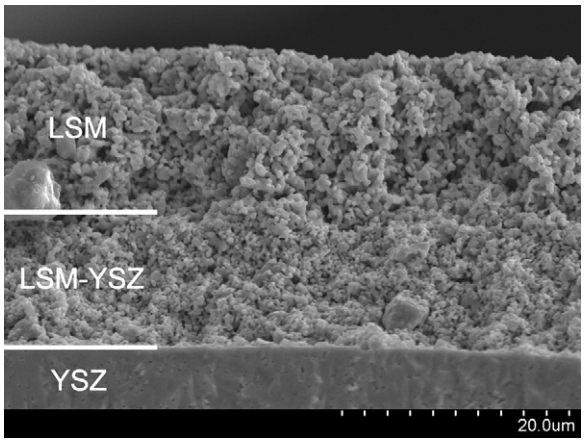

Fig. 1. Cross-sectional SEM image of the LSM and LSM–YSZ layers on top of the dense YSZ electrolyte pellet for the sample with a weight % ratio of 30:70 (LSM:YSZ).

a given set of starting powders, but to improve our understanding of the structural factors limiting cathode performance, including connectivity effects.

The present paper describes results of a combined electrochemical and microstructural study of LSM–YSZ cathodes with composition varied between 30 and 70 wt.% YSZ. While the electrochemical characterization was done using classical impedance spectroscopy measurements on symmetrical cathode samples, microstructural measurements were done using a recently-developed focused ion beam–scanning electron microscopy (FIB–SEM) method that yields quantitative three-dimensional structural information [15–20] and has recently been applied to LSM–YSZ [11]. The observed cathode electrochemical performance versus composition is explained through electrochemical modeling, implementing established techniques for measuring TPB densities, intra-connectivities, and tortuosities to determine the electrochemically-active three-phase boundary (EA-TPB) density [10].

2. Material and methods

2.1. Sample preparation

The samples, consisting of LSM–YSZ cathode layers and LSM current collectors on 8 mol% Y_2O_3-stabilized ZrO_2 (YSZ) electrolyte supports, were prepared as follows [11]. The YSZ electrolyte pellets were prepared by uniaxially dry pressing a mixture of YSZ powder (Tosoh TZ-8YS) and a small amount of PVB binder. The pellets were fired at 1400 °C for 4 h. Identical cathodes were then deposited symmetrically on opposite sides of the pellets using screen printing.

The cathodes were mixtures of LSM (LSM = $La_{0.8}Sr_{0.2}MnO_3$, Praxair) and YSZ, with LSM:YSZ weight ratio varied from 30:70 to 70:30 at intervals of 5%, yielding nine different cathode compositions. The screen printing inks were prepared by first ball milling the LSM and YSZ powder to thoroughly mix, and then combining with a Heraeus vehicle in a three-roll mill. After printing, the LSM–YSZ layers were fired in air at 1175 °C for 1 h. Pure LSM current collector layers were then printed on top of the LSM–YSZ using ink prepared from LSM powder using the procedure noted above. The samples were then fired again in air at 1125 °C for 1 h. Fig. 1 illustrates a fracture cross-sectional scanning electron micrograph (taken using a Hitachi S3400 microscope) of the sample with the 30:70 LSM–YSZ cathode. The LSM–YSZ and LSM layers were both ~10–12 μm thick; the layer thicknesses were consistent (to within 2 μm) throughout the composition series.

2.2. Electrochemical measurements

The symmetric LSM–YSZ cathode samples were electrochemically characterized using a Zahner IM6 electrochemical testing station. For each composition at least three identical samples were fabricated from which the sample with the best performance was used in this study. The sample-to-sample performance variation was <10%.

2.3. FIB–SEM measurements

Image sets were collected with a Zeiss XB 1540 EsB FIB–SEM. These images included the full width of the LSM–YSZ functional layer, along with a portion of the YSZ electrolyte and the LSM current collector. For the purposes of this study, the images were cropped to include only the LSM–YSZ functional layer. This allowed determination of averaged structural properties from the image volume that were characteristic of the LSM–YSZ composite material. Note that for composite electrodes, it is generally understood that the electrode volume rather than the electrode/electrolyte interface dominates the electrochemical properties [21]. For example, the three-phase boundary (TPB) density within the volume of a LSM–YSZ functional layer is expected to largely determine the polarization behavior, with the TPB density at the interface playing a minor role [22]. This assumes that there are not significant structural anomalies at the interface, such as poor interfacial contact, that might impact the electrochemistry. Examination of the present images did not indicate any such interfacial anomalies.

The present FIB–SEM measurements utilized two measures to produce high quality LSM–YSZ three-dimensional images, as discussed previously [11]. First, the pores within the electrode structure were filled with an impregnating epoxy prior to the measurements to allow for better planar sectioning and to make identification of the pore phase easier during the automatic image processing. Second, contrast between the LSM and YSZ phases was achieved by using low electron beam energy and an energy-selective (biased) in-lens backscatter (EsB) detector. The clear contrast between the LSM, YSZ, and pore/epoxy and the uniform contrast within each phase allowed the use of automated procedures to rapidly segment (assign each material phase a specific uniform color) the images for all samples. As a result, the time required for processing an entire set of images for one reconstruction (200–500 images) is reduced to 1–2 h. While it is commonly thought that FIB serial sectioning is a time-consuming and labor-intensive process, the image collection is also an automated procedure and takes only ≈4 h to conduct. With the addition of the time required to align the images, the total time for the entire procedure, starting with FIB sample preparation and ending with a full reconstruction with calculated microstructural data, is on the order of 1–2 days.

The resolutions and volumes of material analyzed differed slightly between samples. In all cases, the resolution was <50 nm in the *X*–*Y* directions (in the plane of the individual 2D images) and in the *Z*-direction (perpendicular to the 2D image planes, *i.e.,* the sectioning direction). The volumes reconstructed were a function of the quality of the imaging conditions, where effects such as shadowing from side walls required different levels of image cropping. In all cases, however, the total volume analyzed for each sample was >500 μm^3; this volume has previously been found to provide sufficient statistics to provide reasonably accurate quantitative data that are representative of the total electrode, for electrodes with these feature sizes [11,15].

2.4. Microstructure calculations

The procedures for performing phase connectivity [10] and tortuosity [15] calculations on the reconstructed microstructure have been published previously. To summarize, the tortuosity is calculated by converting the 3D structure of the phase of interest into a finite-element mesh that is solved for the steady-state diffusion equation. Mean field boundary conditions are implemented in order to reduce any effects from the sample volume boundaries. The intra-connectivity of a given phase is characterized by identifying all networks that are *isolated* within the sample volume, those that are *unknown*, *i.e.,* they appear isolated but intersect one of the boundaries such that the portion outside the measured volume has unknown connectivity, and those that are *connected* throughout the structure. Once the connectivity status of each of the particle networks is labeled, the information can be used in conjunction with the TPB calculation in order to determine the electrochemically-active TPBs, defined as those that touch three intra-connected (percolated) phases of pore, LSM, and YSZ, respectively.

TPB density calculations have also been reported previously [11,15]. The calculation is straightforward: TPB's are identified as voxel edges in contact with voxels of all three phases. However, when a TPB line is at an oblique angle to the cubic voxel edges, it is approximated in the 3D data set as a zig-zag series of orthogonal segments, effectively over-estimating the TPB density. Kenney et al. acknowledge this difficulty in a recent publication where they calculate TPB density from an electrode structure modeled by arrangement of randomly overlapping spheres [23]. Instead of adding the orthogonal TPB line segments defined by voxel edges, they revert to directly calculating the TPB for each solid particle–particle overlap based on the center positions and radii of each particle. While this is certainly a valid method for microstructures defined by spheres, this method cannot be used on reconstructed experimental microstructures with orthogonally defined voxels. Thus, a correction factor was determined to provide more accurate TPB densities. The correction factor for a given short length of TPB line is simply the total length of the orthogonal voxel edge segments, that approximates the TPB in the 3D image, divided by the actual TPB line length. For example, if a TPB happens to run at a 45° angle in the *X*–*Y* plane, the correction factor η is the sum of the *X* and *Y* orthogonal vectors divided by the actual length, or $\eta = \sqrt{2}$. The average value $\langle\eta\rangle$ of the correction factor is obtained by averaging over all TPB angles in 3D space. That is, η is integrated over the surface (S) of a sphere to ensure every angle is counted only once, and dividing this integral by the surface area of the sphere to find the average value. The integral is first set up in Cartesian coordinates:

$$\langle\eta\rangle = \frac{\int_S (X+Y+Z)/\sqrt{X^2+Y^2+Z^2}}{\int_S dS} \quad (1)$$

Converting to polar coordinates and defining the sphere surface as ($\rho = 1$) in the octant of space where *X*, *Y*, and *Z* are all positive (θ and φ go from 0 to $\pi/2$) gives:

$$\langle\eta\rangle = \frac{\int_0^{\pi/2}\int_0^{\pi/2}(\sin\phi\,\cos\theta + \sin\phi\,\sin\theta + \cos\phi)(\sin\theta)(\rho^2)d\theta d\phi}{\int_0^{\pi/2}\int_0^{\pi/2}(\sin\theta)(\rho^2)d\theta d\phi}$$

$$= \frac{\pi/4 + 3/2}{\pi/2} \approx 1.455 \quad (2)$$

Hence, in the results given below, the TPB densities were obtained by adding voxel edge lengths in the 3D data set and then dividing by 1.455.

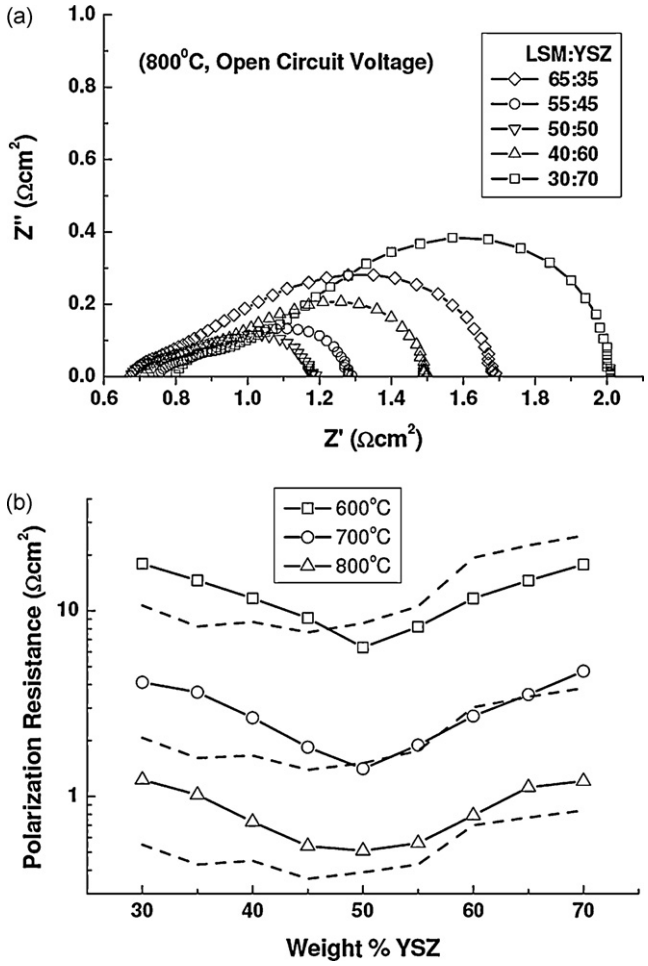

Fig. 2. (a) Nyquist plot of the impedance responses for selected cathode compositions measured at 800 °C in air. The approximate peak frequencies of the two arcs for each sample are as follows: 8.66*E*+03 Hz, 1.33*E*+01 Hz (65:35); 1.15*E*+04, 3.16*E*+01 (55:45); 6.55*E*+03, 1.78*E*+01 (50:50); 6.55*E*+03, 2.37*E*+01 (40:60); and 6.55*E*+03, 4.22*E*+01 (30:70). (b) The cathode polarization resistance at three different temperatures for each composition, extracted from the impedance measurements shown in (a). The dashed lines represent predicted cathode polarizations from electrochemical modeling described in Section 4.2.

3. Results

3.1. Electrochemical characterization

Fig. 2a shows a Nyquist plot illustrating the impedance response of selected cathode samples measured in air at 800 °C with no applied dc voltage. The arcs for 700 and 600 °C are omitted, but maintain the same general shapes as those shown here. The shapes of the impedance arcs are similar to those reported previously for LSM–YSZ cathodes [13], and the interpretation of the data is assumed to be similar to that given in prior work. Here we focus on the total cathode polarization resistance R_P, obtained from the data by taking the difference between the two real axis intercepts of the arcs shown in Fig. 2a. Fig. 2b shows the R_P values for all the cathodes measured at three different temperatures. The 50 wt.% YSZ cathode showed the lowest R_P, with the resistance increasing quite symmetrically as the composition deviated from this value. These results are consistent with those achieved by Haanappel et al., who also varied LSM–YSZ composition through a range of 30–70 wt.% LSM [12]. The activation energies of R_P show no clear trend with cathode composition, falling in a relatively narrow range from 1.03 eV to 1.14 eV. The magnitudes of the R_P values were in the range normally observed for LSM–YSZ composite cathodes measured in this

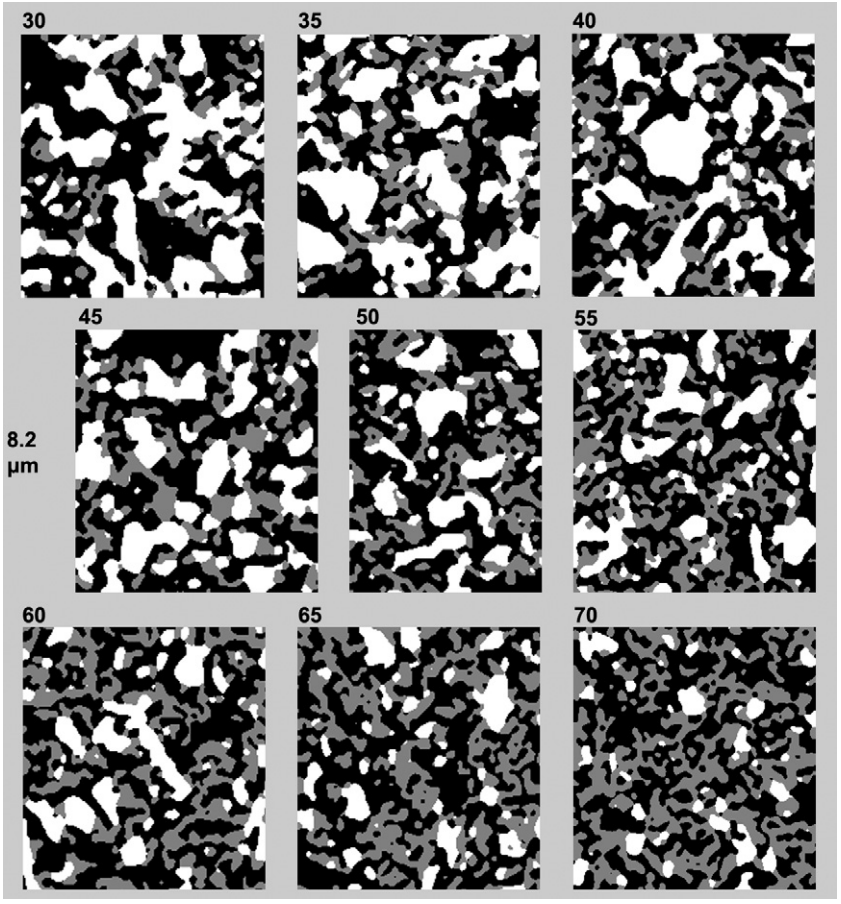

Fig. 3. Segmented 2D images from each composition, labeled by weight % of YSZ. LSM is white, YSZ is grey, and porosity is black. Each image is 8.2 μm tall.

way [13,24]. This is perhaps not surprising given that the starting powder sources and processing procedures used here are fairly common. Thus, the present microstructural results are expected to be fairly representative of LSM–YSZ cathodes studied by many groups.

3.2. Structural characterization

Fig. 3 shows representative fully-segmented two-dimensional images for selected cathode compositions, labeled by the wt.% YSZ. Three different colors were used for the three phases: LSM is white, YSZ is grey, and porosity is black. Visual representations of the full reconstructed 3D volumes are shown in Fig. 4 for selected cathodes. The LSM phase is yellow, the YSZ phase is pink, and the porosity fully transparent. Qualitatively, the amounts of LSM and YSZ appeared to agree with the planned compositions, while the amount of pore phase appears to remain approximately constant. Additionally, the LSM particle size appeared to be significantly larger than that of YSZ, in agreement with the larger average particle size of the LSM starting powder (≈3.0 μm) compared to that of the YSZ powder (≈0.5 μm) [25]. The average pore size appears to become smaller as the cathodes became more YSZ rich, due to the smaller average YSZ particle size.

3.3. Volume and surface area

A number of averaged microstructural parameters were extracted from the 3D data sets, and the data are summarized in Fig. 5. It is important to have sufficient 3D image volume to obtain accurate data. Analysis of the variations in average microstructural quantities as a function of the LSM–YSZ reconstructed volume, similar to the method published previously [16], showed that volumes above 500 μm^3 yielded an error <2%. Fig. 5a shows the total volume reconstructed for each sample. The values varied from ~500 to 1500 μm^3 depending on the size of the segmentable serial-sectioned data set, such that they all met the criterion for yielding reasonably accurate structural data. Note, however, that the minimum volume is dependent on the feature sizes of the composite phases, and will be different for microstructures with larger or smaller feature sizes.

Fig. 5b shows the measured volume percentages of each phase versus wt.% YSZ. While volume % and weight % are effectively interchangeable with respect to sample labeling, for the sake of consistency, starting weight percentage of YSZ is used throughout this paper in order to identify samples. The pore volume did not change significantly with composition. This can be explained by noting that the solids-loadings of the screen-printed inks were all the same, yielding similar packing densities of the green cathode layers, and assuming that neither the LSM nor the YSZ underwent significant sintering shrinkage during cathode firing (1175 °C for 1 h). The dashed lines represent the expected YSZ and LSM volume percentages calculated based on the starting weight % of each phase and the measured average porosity of 50%. As can be seen, the measured YSZ and LSM volume fractions agreed well with the expected values. This provided a good internal test showing that the specific cathode volumes measured were representative of the total electrodes, suggesting that the processing was uniform and consistent, and that the segmentation process was accurate.

The LSM, YSZ, and pore surface area densities (normalized to the *sample* volume) are plotted versus wt.% YSZ in Fig. 5c. The YSZ

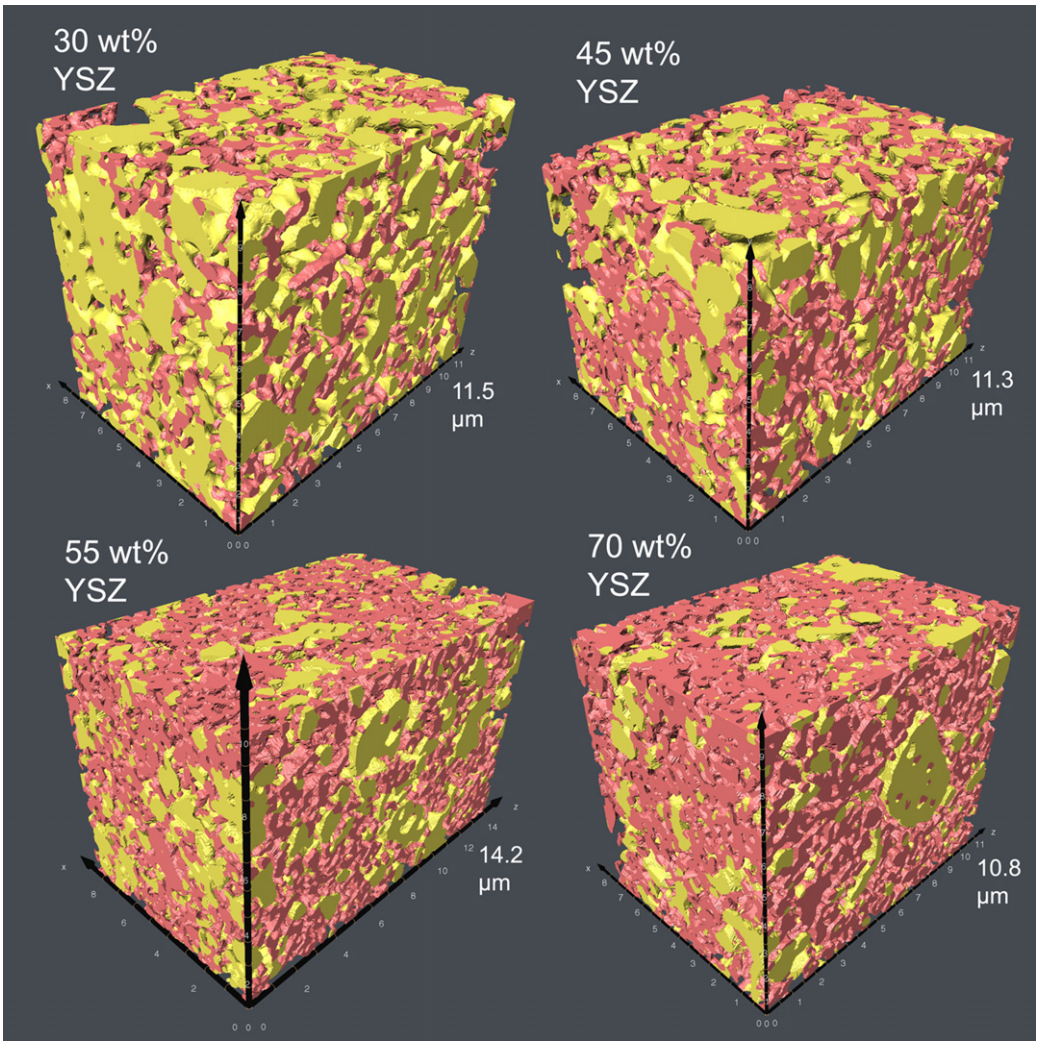

Fig. 4. Visual representations of the full 3D reconstructions of selected cathodes, labeled by weight % YSZ. LSM is yellow and YSZ is pink, while the porosity is transparent. The length of one axis of each reconstruction is labeled for scale, where the total volume of each reconstruction can be found in Fig. 5a.

surface area density increased with increasing wt.% YSZ, while the LSM surface area density showed the opposite trend, as expected from the variations in LSM and YSZ volumes shown in Fig. 5b. The dashed lines are fits to these dependences assuming fixed specific surface areas (surface area divided by *phase* volume) of 12.6 μm^{-1} for YSZ and 7.9 μm^{-1} for LSM. Note that the dashed lines are not perfectly straight because they are based on the measured *volume %* of each phase, not the weight % used in the *X*-axis. The reasonably good agreement with the data versus composition indicates that specific surface area did not vary greatly with cathode composition. The larger specific surface area of YSZ agrees with the visual observations of smaller YSZ particles in Figs. 3 and 4. The pore surface area increased with increasing wt.% YSZ; this can be explained by noting that the pore surface area is defined by the predominant solid phase, such that for cathodes rich in the higher-surface-area YSZ phase, the pore surface area is higher.

3.4. Intra-connectivity

The intra-connectivity of each of the three phases was assessed. The pore phase was found to be 100% percolated for all samples, not surprisingly given that it made up 50% of the volume of the cathodes. As a result, the pore phase is taken to be 100% intra-connected in the following analyses. Fig. 6 shows 3D visual representations of the isolated (red) and unknown (blue) particle networks of LSM (a) and YSZ (b) for three cathode compositions. Fig. 7a shows the measured volume fraction of connected YSZ and LSM in the cathodes versus wt.% YSZ, which quantifies the trends that can be seen in Fig. 6. The values were achieved by assuming that "unknown" networks were either isolated or connected with respect to the cathode volume outside our image area, in the same proportion as that measured within our sample volume. For reference, error bars are included that represent the maximum and minimum possible levels of connectivity, spanning the full volume % measured as "unknown". The YSZ phase was almost fully connected down to 45 wt.% YSZ (25 vol% YSZ), and the connectivity dropped to 94% at 30 wt.% YSZ (only 14.6% YSZ by volume). The LSM phase showed substantial decreases in its connectivity as the wt.% YSZ increased, down to <60% connected for >60 wt.% YSZ. The dashed lines shown are the results of structural modeling, discussed in Section 4.1, that also helps to explain the reasons for the much-different intra-connectivities of LSM and YSZ.

3.5. Three-phase boundary density

Volumetric TPB densities are plotted versus wt.% YSZ in Fig. 7b. The total TPB density is skewed toward the LSM-rich side. TPB densities ranged from 6 to 9 μm^{-2}; these values are greater than those obtained from FIB-SEM measurements of Ni-YSZ *anodes* [26], presumably due to the comparatively finer microstructure of the

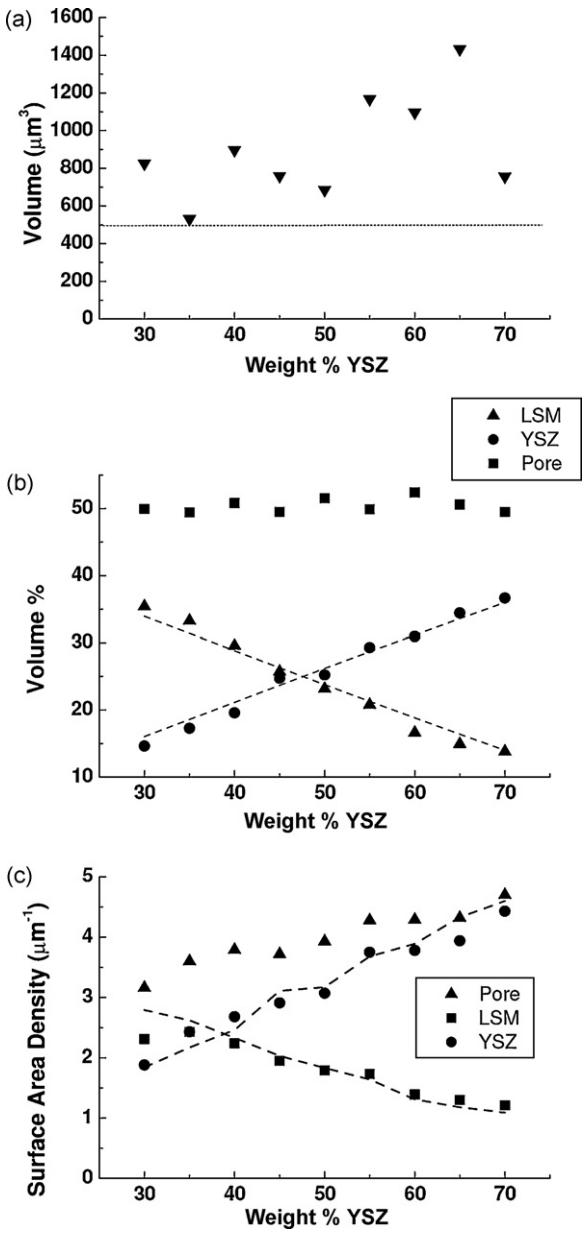

Fig. 5. Averaged cathode structural data plotted versus composition. (a) The total volume of electrode reconstructed for each sample, with the minimum volume of 500 μm^3 for <2% error shown by the dashed horizontal line. (b) The volume percentages of each phase measured from the 3D reconstructions. The dashed line represents the expected values based on the starting weight ratios of LSM to YSZ. (c) Surface area densities of each phase; the dashed lines showing the surface area densities expected for constant specific surface areas for the LSM and YSZ phases.

present electrodes. Comparison of the composition dependences of the total TPB density in Fig. 7b with the R_P values in Fig. 2 show no apparent correlation. This suggests that factors other than the TPB density influenced R_P. One such factor is the phase intra-connectivity shown in Fig. 6. This information yielded the electrochemically-active TPBs (EA-TPBs), using the criterion that the TPB had to be on connected LSM, YSZ, and pore networks in order to be active. Fig. 8 shows 3D visual representations of the TPBs for 5 of the 9 compositions, with active TPBs in green, TPBs of unknown activity in blue, and inactive TPBs in red. The influence of the unconnected LSM particle networks is apparent, as the amount of active (green) TPBs dramatically decreased as the LSM content decreased. Fig. 7b shows the resulting measured EA-TPB densities versus wt.% YSZ. Due to the high levels of unconnected LSM at high YSZ content, the EA-TPB density is less than half of the total TPB density. There was relatively minimal effect at the lowest YSZ content due to the high YSZ connectivity noted above.

3.6. Tortuosities

The cathode pore phase tortuosity τ is of interest because it can impact concentration polarization losses [27]. The tortuosity of the YSZ phase is also considered here because it can impact ionic transport within the YSZ phase of the LSM–YSZ composite [26]. The LSM tortuosity was not considered because electron transport was not expected to limit cathode performance, based on the relatively high electronic conductivity of LSM and the relatively low LSM–YSZ layer thickness. Fig. 7c shows a plot of the pore and YSZ tortuosities versus cathode composition. A pore tortuosity $\tau \approx 1.6$ was observed independent of composition; cathode tortuosities have not been characterized, but this value is at the lower end of the range normally observed or assumed for SOFC anodes [28,29].

The YSZ phase showed a rapid increase in τ with decreasing YSZ content, reaching a quite high value of 6.5 for 30 wt.% YSZ. This high τ value may be explained by the long path lengths required to circumnavigate the high density of LSM networks at low YSZ content. These τ values are higher than for standard Ni-YSZ anodes, presumably a function of the finer microstructure and lower volume percentages of YSZ that is found in the cathodes, compared to the composite anodes [30]. This is most likely a direct result of the fact that the cathodes are only partially sintered, producing higher porosity and hence lower overall YSZ volume, while the Ni-YSZ anodes are fully sintered before the porosity is produced from reduction of NiO to Ni.

Characteristic particle diameters can be estimated from microstructural features. If a phase is fully connected, it is expected that the structure would best be described by a series of interconnected tubes whose volume to surface area ratio is equal to 4. If a phase consists entirely of isolated spheres, its volume to surface area ratio would equal 6. In reality, electrode structures usually consist of a combination of connected tube-like structures and isolated spherically shaped particles. The level to which each type of shape contributes to the overall microstructure is estimated based on the connectivity calculations for each phase, where active volume is treated as tubes and isolated phases are treated as spheres. As a result, the characteristic diameter of a real microstructure is estimated to be equal to the ratio of the volume to surface area times the linear extrapolation of the amount of isolated phase between the values of 4 and 6. Calculating the characteristic diameter for each composition based on the measured volumes (Fig. 5b), surface areas (Fig. 5c), and % of connectivity (Fig. 5e), yielded an average diameter of $0.56 \pm .04$ μm for LSM and $0.32 \pm .02$ μm for YSZ, very consistent values independent of composition.

3.7. Interfacial curvatures

Detailed analysis of the surface curvature of each phase can also be used to calculate the type of curvature that is dominant within the structure, revealing the prevailing shape of the particle networks [31,32]. The curvature is analyzed by first using software to describe the surface of the phase as a continuous network of triangles and their vertices, a common technique in 3D analysis. The surface directly surrounding each vertex is analyzed to determine its two radii of curvature, R_1 and R_2, and this procedure is repeated for all vertices of the structure as described elsewhere [31]. A summation of this data is presented in Fig. 9, which plots the probability (indicated by color) of each combination of curvature values $\kappa_1 = (1/R_1)$ and $\kappa_2 = (1/R_2)$. The diagram in the upper left section of Fig. 9 illustrates schematically the types of curvature to

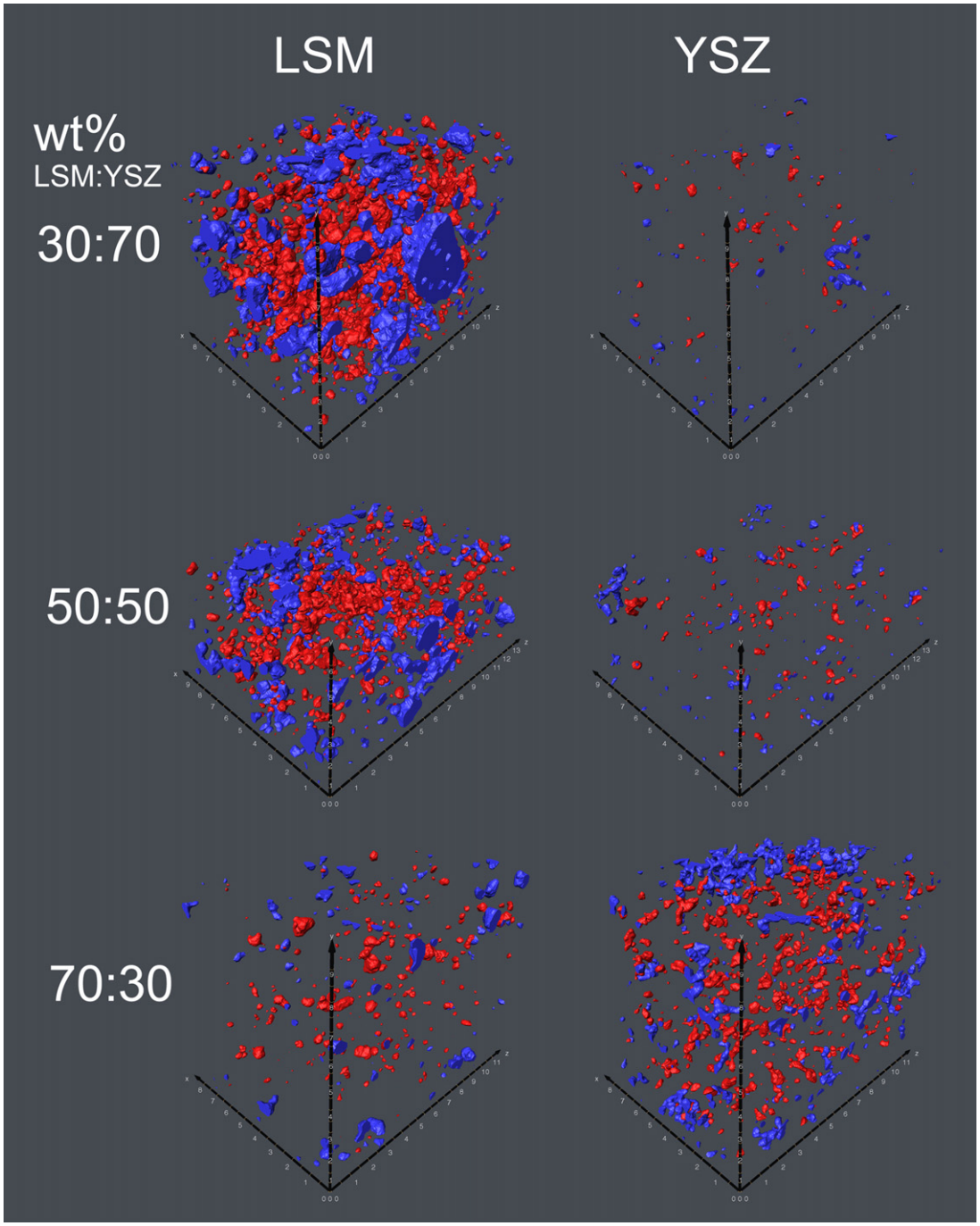

Fig. 6. Three-dimensional visual representations of the isolated (red) and "unknown" (blue) particle networks for the LSM and YSZ phases for three selected compositions. (For interpretation of the references to color in this figure legend, the reader is referred to the web version of the article.)

which each region of the interfacial shape distribution (ISD) correspond [33]. Note that the distance between the origin and the curvature probability maximum, shown in red in the plots in Fig. 9, corresponds to the inverse of the most probable network feature radius.

A typical example of the pore phase curvature data is shown for the 50 wt.% YSZ cathode in Fig. 9. The data for the pore phase showed little variation in the shape of the plot with wt.% YSZ, staying centered on a saddle-type curvature. However, the location of the peak (red) continuously moved further from the origin as YSZ content increased, implying that the feature size of the pores continuously decreased. This is in agreement with Fig. 5c, which showed that the pore phase surface area increased with increasing YSZ content. Fig. 9 also shows an example of the LSM phase in a 50 wt.% YSZ cathode; the highest probability was centered at a solid-inside cylinder. The LSM phase showed a slight change from "saddle" shaped curvature to "cylindrical" type curvature with increasing wt.% YSZ. This is somewhat surprising considering that the LSM phase moves from a fully connected structure at low W_{YSZ} to one that is more than half (by volume) isolated networks at high W_{YSZ}. With this type of structural change, one would expect that the structure dominated by isolated networks would consist mostly of curvature with positive R_1 and R_2 values (approximately spherical), though the data showed mostly cylindrical curvature. The reason for this result is unclear, although it could be due to surface roughness on the large LSM particles that averages out most

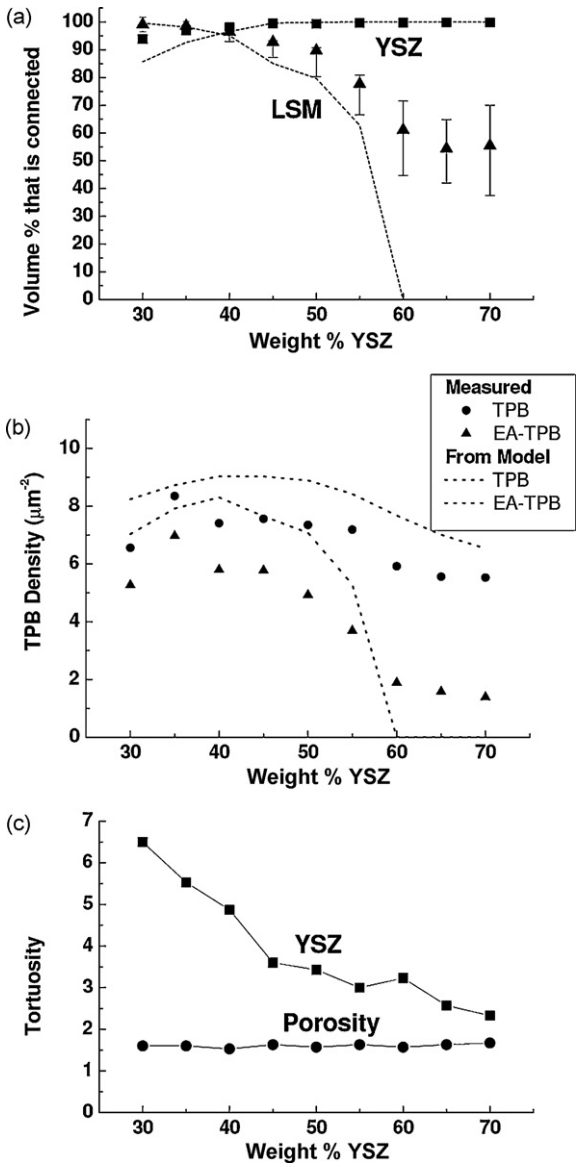

Fig. 7. (a) Measured level of connectivity of the YSZ and LSM phases as a percentage of the total phase volume. The error bars represent the full range of possible connectivity depending on what proportion of the "unknown" particle networks are assumed to be isolated. The dashed lines represent the values estimated using the Zhu et al. model. (b) The measured TPB and EA-TPB densities plotted versus weight % YSZ. TPB and EA-TPB densities estimated using the Zhu et al. model are shown as dashed lines for comparison. In the model, particle diameters of 0.56 μm for LSM and 0.32 μm for YSZ were used, while the particle contact angle is assumed to be 15°, and an average coordination number of 6 is used. (c) Average tortuosity values for the YSZ and pore phases.

of the spherical curvature. The YSZ phase showed the most change throughout the range of compositions. Fig. 9 shows the YSZ curvature plots for cathodes with 70, 50, and 30 wt.% YSZ. It can be clearly seen that the YSZ phase moves from a mostly saddle-type curvature at high YSZ content, as one would expect for a highly contiguous, high volume % structure, to a structure with mostly cylindrical type (solid-inside) curvature. The latter is perhaps not surprising considering the fact that for the 30 wt.% sample to maintain such high intra-connectivity at such low volume % it must consist mostly of connected tubes of YSZ. Overall, while the curvature calculations in this case are used to reinforce other methods of structural analysis, they can prove to be very useful in future degradation studies that analyze morphological changes due to coarsening [34].

4. Discussion

4.1. Effect of composition on connectivity and TPB density

The measured total TPB density showed a maximum skewed towards an LSM-rich composition. This can be understood quantitatively using composite electrode structural models that estimate TPB densities as a function of volume fractions and particle sizes based on random packing of spherical particles [14,23,35,36]. Fig. 7b shows a comparison of the measured and estimated total TPB densities, the latter based on the Zhu et al. model [14]. The magnitude of the estimated TPB curve agrees reasonably well with the measured total TPB densities considering that no fitting parameters were employed – the volume percentages and the characteristic diameters determined in section 3.3 were used in the model along with other parameters suggested by Zhu et al. [14], a particle contact angle of 15° and an average coordination number of 6. The model predicts that the magnitude of the TPB densities increases with decreasing particle sizes; that is, if both types of particles are made smaller, their higher surface areas will give rise to higher TPB densities. For example, the predicted curve in Fig. 7b can be made to match the experimental TPB densities by increasing both particle sizes by ≈9% from their measured values.

The *shape* of the model prediction also agrees well with the experimental TPB results, with the TPB maximum occurring at an LSM-rich composition. In the model, the ratio of the characteristic diameters determines the TPB maximum. The skewed maximum can be understood by noting that the maximum opportunity for making TPB's occurs when the two phases have equal surface areas, which requires a larger volume fraction of the larger-feature-size phase.

The structural model can also address electrochemically-active TPB densities, the subset of the total TPB density where the phase intra-connectivity requirement is met for all three phases. For the EA-TPB calculation, the same structural model was used, but a percolation theory expression was included to calculate the probability f_C that a particle is part of a percolated network [14,37],

$$f_C = \left[1 - \left(\frac{(4.236 - Z)}{2.472}\right)^{2.5}\right]^{0.4} \quad (3)$$

where Z is the coordination number between same-phase particles and is a function of the particle radius and volume percentage for each phase. Fig. 7a shows the values calculated using Eq. (3) as dashed lines, which agree quite well with the measured intra-connected fractions f_C of LSM and YSZ. The only serious discrepancy is at >60 wt.% YSZ (LSM *volume* fraction <0.2), where the measured $f_{C,LSM}$ is substantially greater than the predicted value of zero. This is probably due to the model assumption that all LSM particles have equal sizes, whereas in reality there is significant width to the particle size distribution. The much lower intra-connectivities of LSM compared to YSZ can be understood based on the idea that there is a lower number density of the larger LSM particles, compared to the same volume of smaller YSZ particles, which leads to a smaller Z value. Thus, at equal volume fractions LSM and YSZ, there is a higher probability of a YSZ particle having at least one YSZ neighbor – leading to high connectivity – and a lower probability of a LSM particle having at least one LSM neighbor – leading to lower connectivity. The calculated EA-TPB density $\rho_{EA\text{-}TPB}$ was related to the calculated total TPB density ($\rho_{T\text{-}TPB}$) by the expression

$$\rho_{EA\text{-}TPB} = \rho_{T\text{-}TPB} f_{C,pore} f_{C,LSM} f_{C,YSZ} \quad (4)$$

where $f_{C,pore} \approx 1.0$ for all compositions as discussed in Section 3.4.

Fig. 7b shows that there was general agreement between the measured EA-TPB densities and the prediction of Eq. (4). The most

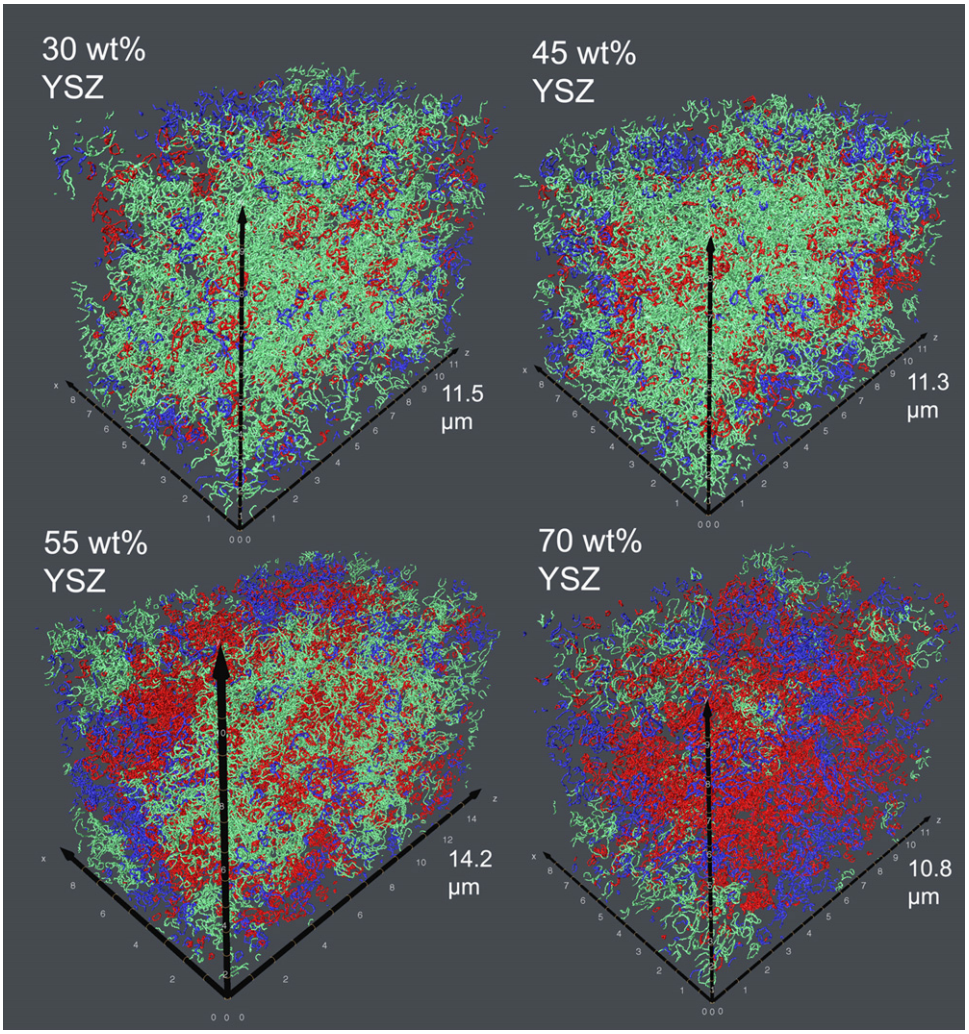

Fig. 8. Three-dimensional visual representations of the TPB segments for four selected compositions, with the active TPB's in green, the TPB's of unknown activity in blue, and the in-active TPB's in red. The length of one axis of each reconstruction is labeled for scale, where the total volume of each reconstruction can be found in Fig. 5a. (For interpretation of the references to color in this figure legend, the reader is referred to the web version of the article.)

significant effect was due to low LSM intra-connectivity at the YSZ rich compositions. The main discrepancy between the measured and calculated EA-TPB density was at low LSM content, where the predicted $\rho_{\text{EA-TPB}} \to 0$; this arises because $f_{\text{C,LSM}} \to 0$ as discussed above. Overall, however, the present data supports the idea that sphere-packing structural models can provide reasonable predictions of TPB densities, at least for powder-processed composite cathodes with relatively high porosity.

4.2. Effect of microstructure on polarization resistance

A simple calculation based on the Tanner–Fung–Virkar (TFV) composite electrode model [38] was employed to predict R_P based on the measured microstructures. The TFV model accounts for oxygen ion transport in the ionically-conducting phase (YSZ in the present case) by assuming that it consists of one-dimensional columns aligned normal to the cathode/electrolyte interface. The effect of the cathode electronically-conducting phase (LSM in the present case), and in particular the associated TPB's, is approximated as an average surface resistance R_S on the ionically-conducting column surfaces. A tacit assumption of this model is that all phases are fully contiguous and that both concentration polarization and ohmic resistances within the LSM phase are negligible.

In the present calculations, a model cathode was set up for each LSM–YSZ composition based on the measured structural data (see Section 3). The YSZ column width L_{YSZ} was set as the measured YSZ-phase diameter. A YSZ conductivity value of 0.021 S/cm at 800 °C was used; note that this value is for Mn-doped YSZ (as expected in a LSM–YSZ cathode), and is ~3 times that for pure YSZ [39,40]. The distance L_{Pore} between the YSZ columns was set such that the YSZ volume fraction in the model cathode was equal to the measured value for that composition. An electrode thickness was set at 12 μm, an average of the measured cathode functional layer thicknesses. The TPB's were taken to be uniformly distributed on the YSZ column surfaces, with an area-specific density $\rho^{\text{A}}_{\text{EA-TPB}}$ given by

$$\rho^{\text{A}}_{\text{EA-TPB}} = \frac{\rho_{\text{EA-TPB}}\,\Lambda}{2}, \tag{5}$$

where $\Lambda = L_{\text{YSZ}} + L_{\text{Pore}}$ is the period of the YSZ columns and $\rho_{\text{EA-TPB}}$ is the volume TPB density. The average surface resistance R_S was calculated as the product of this area-specific TPB density and the resistance R_{TPB} associated with a unit length of TPB, such that

$$R_S = \frac{R_{\text{TPB}}\rho_{\text{EA-TPB}}\,\Lambda}{2}. \tag{6}$$

R_{TPB} was used as a fitting parameter below, where a constant value was chosen to match the modeled R_P result with the measured R_P value for the 50 wt.% YSZ cathode. For the LSM–YSZ cathode sys-

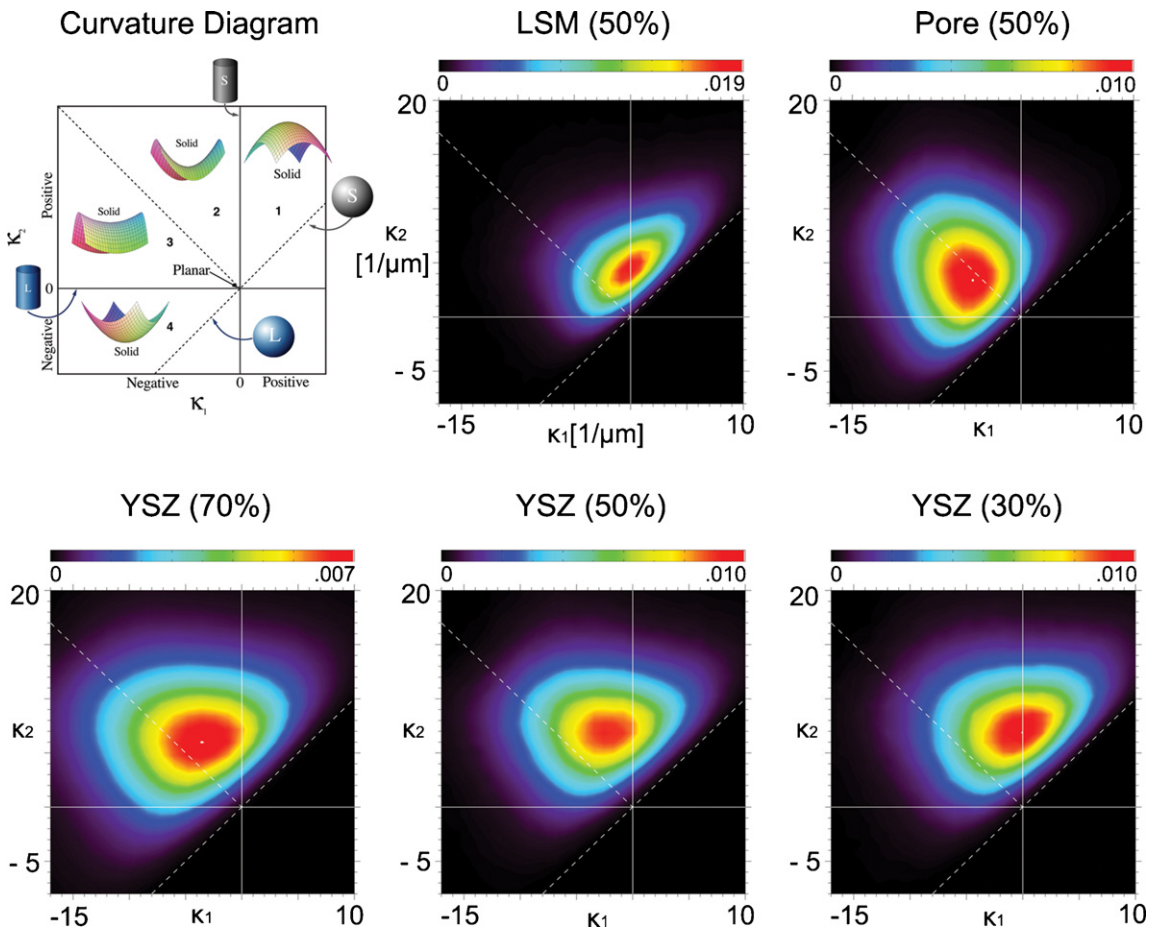

Fig. 9. The upper left diagram shows the different regions of the κ_1–κ_2 plot and to what types of curvature these regions correspond [34]. The others are interfacial shape distributions for each of the LSM, YSZ, and pore phases, colored by the level of probability for each curvature combination within the structure.

tem in this study, a constant value of $R_{TPB} = 1.9 \times 10^5\ \Omega\,cm$ at 800 °C was determined in this manner and is subsequently compared with previous measurements from literature [41].

Fig. 10 shows calculated polarization resistance R_P values versus cathode composition compared to the measured data, both at 800 °C. For purposes of illustration, the calculation was done first using the *total* TPB density in Eq. (6) (dotted line in Fig. 10). This yielded an R_P value that varied little with composition, and that bore little resemblance to the measured data. That is, when

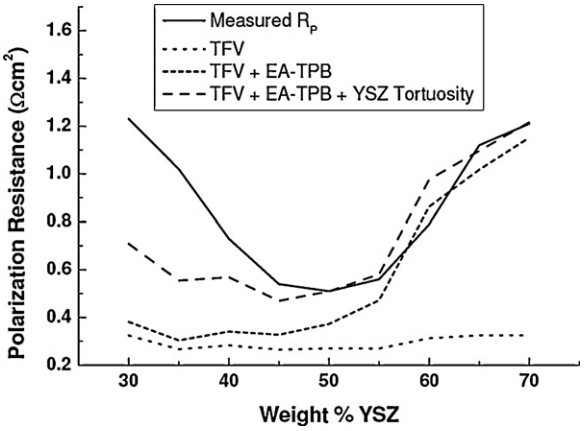

Fig. 10. Measured and estimated polarization resistances at 800 °C for composite LSM–YSZ cathodes using the TFV electrochemical model for different compositions and model parameters, with $R_{TPB} = 1.9 \times 10^5\ \Omega\,cm$.

connectivity effects were ignored, the agreement was poor. Using the electrochemically-active TPB density provided better agreement with the measured data (short-dashed line in Fig. 10), particularly at high wt.% YSZ, where the low intra-LSM connectivity substantially increased the predicted R_P. For example, for 70 wt.% YSZ, only 55 vol% of the LSM was intra-connected, such that $\rho_{EA\text{-}TPB} = 1.39\ \mu m^{-2}$ compared to $\rho_{T\text{-}TPB} = 5.53\ \mu m^{-2}$, increasing R_P to $0.897\ \Omega\,cm^2$ compared to the value of $0.246\ \Omega\,cm^2$ obtained using the total TPB density. On the other hand, connectivity effects did not explain the high polarization resistances measured at low YSZ content, because the YSZ showed high connectivity at all compositions.

The high polarization resistance at low YSZ content can potentially be explained by bulk ionic transport limitations. Such an effect should become more pronounced as YSZ content decreases, both because the amount of YSZ available for oxygen ion transport decreases and because the YSZ tortuosity increases (Fig. 7c). YSZ tortuosity was implemented in the R_P calculations by dividing the YSZ conductivity by the tortuosity factor. This serves as a correction to the TFV model, which assumes straight-through pathways for ion transport in YSZ columns, for the actual tortuous ion pathways in the real cathodes. The predicted R_P including the YSZ tortuosity, shown as the long-dashed line in Fig. 10, provides better agreement with the measured composition dependence. Overall, the agreement is reasonable, perhaps as good as can be expected given the simplified structure assumed in the calculations, compared with the actual complex microstructure. Furthermore, the R_{TPB} values obtained in the fits $-1.9 \times 10^5\ \Omega\,cm$ at 800 °C, $5.5 \times 10^5\ \Omega\,cm$ at 700 °C, and $28.7 \times 10^5\ \Omega\,cm$ at 600 °C – were in reasonable agree-

ment with values obtained in a prior patterned electrode study – $1.26 \times 10^5\ \Omega$ cm at 800 °C, $6.13 \times 10^5\ \Omega$ cm at 700 °C, and an extrapolated value of $42.3 \times 10^5\ \Omega$ cm at 600 °C [41]. They are also in fair agreement with the value $R_{TPB} \approx 1.0 \times 10^5\ \Omega$ cm at 800 °C reported based on stereological calculations [9]. The results of the full TFV modeling when using the R_{TPB} patterned electrode values from literature are plotted as dashed lines in Fig. 2b, as comparison to the measured data. The modeled polarizations fit reasonably well in magnitude with the experimental values at 700 °C, however they are slightly off with respect to the 600 °C and 800 °C values. This is a function of the fact that the activation energy of R_{TPB} from the patterned electrode study was ≈1.42 eV, where our experimental value was ≈1.08 eV. This is most likely due to the differences in processing, starting materials, and impurities that highlight the difficulties in comparing patterned electrode results to those of composite electrodes from different laboratories.

A number of model simplifications probably contributed to discrepancies with the experimental data in Fig. 2b. For example, the model treats the discrete TPB reaction sites as a diffuse reaction on the surface of the YSZ. While the density of TPBs on the YSZ may be large enough to allow this approximation (the distance between TPB segments on the YSZ column is approximately half the width of the YSZ column), two studies using microelectrodes have shown that current constriction in the electrolyte at the TPB also adds a resistance to the electrode [42,43]. This effect is ignored in the present calculations and should certainly increase the measured electrode polarization, particularly at low YSZ content where the YSZ pathways are both thin and highly tortuous.

One additional factor that is not considered here is the effect of the contact between the electrode and electrolyte interface. The present reconstructed volumes ended ∼1 μm from the cathode–electrolyte interface, such that any effects at the interface are not included. This expediency was useful for obtaining averaged functional layer structural quantities, and was probably reasonable as the overall number of TPBs in the functional layer was much larger than that expected at the interface. However, it is possible, in principle, that poor contact between the cathode YSZ phase and the YSZ electrolyte could lead to current constriction at the interface. Recent investigations of the cathode–electrolyte interfaces of the present samples did not reveal poor interfacial contact or unusually high interfacial TPB densities [44].

Lastly, the present work has not considered the details of the TPB reaction, which could be limited primarily by kinetics at the TPB itself, or could be limited by processes occurring on surfaces at some distance from the TPB, such as oxygen adsorption and surface diffusion on either or both the LSM and YSZ surface [45]. That is, processes relevant to the oxygen reduction reaction may extend a characteristic distance from the TPB over the adjacent LSM–pore and YSZ–pore interfaces. Some studies have shown that this characteristic distance on LSM is less than 1 μm [46,47]. Oxygen reduction may also occur on the YSZ surface, a result of substantial Mn diffusion across the surface of YSZ in LSM–YSZ systems after activation by extended polarization, over a distance of at least 10 μm [48,49]. The present structural data allows an assessment of the average widths of the LSM–pore and YSZ–pore interfaces adjacent to TPBs in LSM–YSZ composites. These widths can potentially affect the R_{TPB} value. For example, if the measured widths are substantially smaller than the characteristic adsorption/diffusion distances, then the area "feeding" the TPB would be limited, increasing R_{TPB}.

Fig. 11 shows the measured LSM–pore and YSZ–pore interface areas, divided by the EA-TPB length, *i.e.*, the average width of the interface adjacent to TPBs. The LSM–pore interface width was fairly constant at ≈0.27 μm irrespective of composition. The YSZ–pore interface width had a similar value for low YSZ content, but increased substantially for YSZ content increased above 50 wt.%. Note that the value of ≈0.25 μm in Fig. 11 is comparable or less

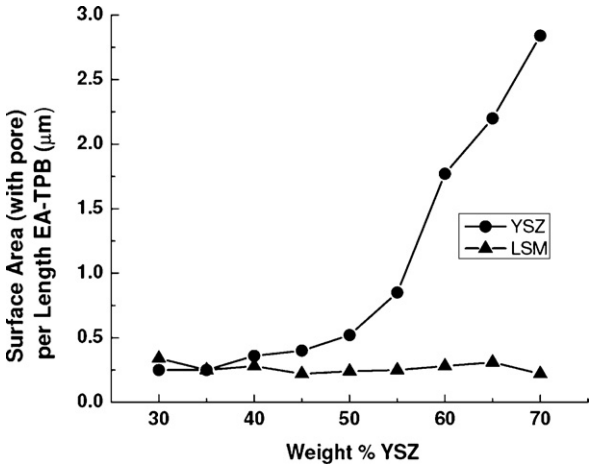

Fig. 11. The electrochemically-active solid-pore surface area per length of EA-TPB for both the LSM and YSZ phases as a function of the starting weight percent of YSZ.

than the estimated characteristic surface-reaction lengths noted above, so it is certainly possible that surface-width limitations play a role in the TPB processes. Further 3D studies of LSM–YSZ composite cathodes with different microstructures may provide additional information about characteristic TPB widths.

5. Conclusions

Serial sectioning using FIB-SEM was implemented to reconstruct the 3D microstructure of nine composite cathodes with compositions ranging from 30:70–70:30 weight % LSM:YSZ. In addition to yielding phase volume fractions, surface area densities, phase tortuosities, and total TPB densities, the levels of connectivity of the phases were analyzed in order to determine the electrochemically-active TPB densities.

Cathode polarization resistances were measured for all of the cathodes, and showed a strong minimum at ∼50 wt.% YSZ. The values were compared with predictions made using a simple composite cathode electrochemical model employing the 3D structural data. Considering only the total TPB densities yielded poor agreement with the composition variation of the measured polarization resistance. However, model predictions using the electrochemically-active TPB densities, and also considering ionic transport limitations in the YSZ phase, yielded much better agreement. In particular, the low intra-connectivity of the LSM phase at low-LSM compositions and the high tortuosity of the YSZ phase at low-YSZ compositions were important factors yielding the observed high polarization resistance at these composition extremes. These results highlight the importance of these microstructural features that can only be quantified using three-dimensional imaging.

The general nature of the present results are expected to be valid for a wide range of LSM–YSZ cathodes. However, as connectivities, tortuosities, and TPB densities are predicted to depend strongly on LSM and YSZ particle size distributions as well as the firing conditions, the specific quantitative results may be substantially different for cathodes made with different processing conditions and particle sizes.

Acknowledgments

The authors gratefully acknowledge the financial support of the National Science Foundation Ceramics program through grants DMR-0542740 (Northwestern Univ.) and 0645812 (UC-Irvine). The authors also acknowledge the use of the facilities within the Carl

Zeiss Center of Excellence at the University of California, Irvine as well as Marcio Gameiro for his work involving the connectivity calculations.

References

[1] S.P. Jiang, J.G. Love, J.P. Zhang, M. Hoang, Y. Ramprakash, Solid State Ionics 121 (1999) 1–10.
[2] M.J. Jorgensen, M. Mogensen, J. Electrochem. Soc. 148 (5) (2001) A433–A442.
[3] Z.G. Lu, Y. Jiang, Y.L. Dong, Y.H. Zhang, J.W. Yan, Chem. J. Chinese U. 22 (2001) 791–795.
[4] T. Tsai, S.A. Barnett, Solid State Ionics 93 (1997) 207.
[5] N.Q. Minh, J. Am. Ceram. Soc. 76 (1993) 563–588.
[6] S. McIntosh, S.B. Adler, J.M. Vohs, R.J. Gorte, Electrochem. Solid State Lett. 7 (2004) A111.
[7] Y.J. Leng, S.H. Chan, K.A. Khor, S.P. Jiang, in: S.C.a.D.M. Singhal (Ed.), 8th International Symposium on Solid Oxide Fuel Cells (SOFC-VIII), 2003.
[8] H. Yokokawa, H. Tu, B. Iwanschitz, A. Mai, J. Power Sources 182 (2008) 400–412.
[9] F. Zhao, Y. Jiang, G.Y. Lin, A.V. Virkar, Solid Oxide Fuel Cell VII (SOFC-VII), 2001.
[10] J.R. Wilson, M. Gameiro, K. Mischaikow, W. Kalies, P.W. Voorhees, S.A. Barnett, Microsc. Microanal. 15 (2009) 71–77.
[11] J.R. Wilson, A.T. Duong, M. Gameiro, H.Y. Chen, K. Thornton, D.R. Mumm, S.A. Barnett, Electrochem. Commun. 11 (2009) 1052–1056.
[12] V.A.C. Haanappel, J. Mertens, D. Rutenbeck, C. Tropartz, W. Herzhof, D. Sebold, F. Tietz, J. Power Sources 141 (2005) 216–226.
[13] E.P. Murray, S.A. Barnett, Solid State Ionics 143 (2001) 265–273.
[14] W. Zhu, D. Ding, C. Xia, Electrochem. Solid-State Lett. 11 (2008) B83–B86.
[15] J.R. Wilson, W. Kobsiriphat, R. Mendoza, H.Y. Chen, J.M. Hiller, D.J. Miller, K. Thornton, P.W. Voorhees, S.B. Adler, S.A. Barnett, Nat. Mater. 5 (2006) 541–544.
[16] J.R. Wilson, W. Kobsiriphat, R. Mendoza, H.-Y. Chen, T. Hines, J.M. Hiller, D.J. Miller, K. Thornton, P.W. Voorhees, S.B. Adler, D. Mumm, S.A. Barnett, Three Dimensional Reconstruction of Solid Oxide Fuel Cell Electrodes Using Focused Ion Beam-Scanning Electron Microscopy Solid Oxide Fuel Cells 10 (SOFC-X), 2007.
[17] D. Gostovic, J.R. Smith, D.P. Kundinger, K.S. Jones, E.D. Wachsman, Electrochem. Solid State Lett. 10 (2007) B214–B217.
[18] J.R. Izzo, A.S. Joshi, K.N. Grew, W.K.S. Chiu, A. Tkachuk, S.H. Wang, W.B. Yun, J. Electrochem. Soc. 155 (2008) B504–B508.
[19] J.R. Wilson, S.A. Barnett, Electrochem. Solid State Lett. 11 (2008) B181–B185.
[20] L. Holzer, F. Indutnyi, P.H. Gasser, B. Munch, M. Wegmann, J. Microsc -Oxford 216 (2004) 84–95.
[21] H. Fukunaga, M. Ihara, K. Sakaki, K. Yamada, Solid State Ionics 86–88 (1996) 1179–1185.
[22] T. Kenjo, M. Nishiya, Solid State Ionics 57 (3–4) (1992) 295–302.
[23] B. Kenney, M. Valdmanis, C. Baker, J.G. Pharoah, K. Karan, J. Power Sources 189 (2009) 1051–1059.
[24] S.P. Jiang, Y.J. Leng, S.H. Chan, K.A. Khor, Electrochem. Solid State Lett. 6 (2003) A67–A70.
[25] M. Trunec, J. Eur. Ceram. Soc. 24 (2004) 645–651.
[26] J.R. Wilson, W. Kobsiriphat, R. Mendoza, H.-Y. Chen, J.M. Hiller, D.J. Miller, K. Thornton, P.W. Voorhees, S.B. Adler, S.A. Barnett, Nat. Mater. 5 (2006) 541–544.
[27] F. Zhao, A.V. Virkar, J. Power Sources 141 (2005) 79–95.
[28] Y. Jiang, A.V. Virkar, J. Electrochem. Soc. 150 (2003) A942.
[29] V.H. Schmidt, C.L. Tsai, J. Power Sources 180 (2008) 253–264.
[30] J.R. Wilson, S.A. Barnett, unpublished work.
[31] R. Mendoza, J. Alkemper, P.W. Voorhees, Metall. Mater. Trans. A 34 (2003) 481–489.
[32] R. Mendoza, I. Savin, K. Thornton, P.W. Voorhees, Nat. Mater. 3 (2004) 385–388.
[33] D. Kammer, P.W. Voorhees, Acta Mater. 54 (2006) 1549–1558.
[34] J.H. Kim, W.K. Liu, C. Lee, Comput. Mech. 44 (2009) 683–703.
[35] D.F. Chen, Z.J. Lin, H.Y. Zhu, R.J. Kee, J. Power Sources 191 (2009) 240–252.
[36] J. Golbert, C.S. Adjiman, N.P. Brandon, Ind. Eng. Chem. Res. 47 (2008) 7693–7699.
[37] M. Suzuki, T. Oshima, Powder Technol. 35 (1983) 159–166.
[38] C.W. Tanner, K.Z. Fung, A.V. Virkar, J. Electrochem. Soc. 144 (1997) 21–30.
[39] K. Yamahara, T.Z. Sholklapper, C.P. Jacobson, S.J. Visco, L.C. De Jonghe, Solid State Ionics 176 (2005) 1359–1364.
[40] T. Kawada, N. Sakai, H. Yokokawa, M. Dokiya, I. Anzai, Solid State Ionics 50 (1992) 189–196.
[41] R. Radhakrishnan, A.V. Virkar, S.C. Singhal, J. Electroch. Soc. 152 (2005) A210–A218.
[42] J.L. Hertz, H.L. Tuller, Solid State Ionics 178 (2007) 915–923.
[43] J. Fleig, Z. Phys. C 221 (2007) 1149–1159.
[44] J.R. Wilson, J.S. Cronin, S. Rukes, A. Duong, D. Mumm, S. Barnett, 11th International Symposium on Solid Oxide Fuel Cells, Vienna, Austria, 2009.
[45] S.B. Adler, Chem. Rev. 104 (2004) 4791–4843.
[46] T. Horita, K. Yamaji, M. Ishikawa, N. Sakai, H. Yokokawa, T. Kawada, T. Kato, J. Electrochem. Soc. 145 (1998) 3196–3202.
[47] F.H. van Heuveln, H.J.M. Bouwmeester, F.P.F. van Berkel, J. Electrochem. Soc. 144 (1997) 126–133.
[48] M. Backhaus-Ricoult, 15th International Conference on Solid State Ionics, Baden, Germany, 2006.
[49] M. Backhaus-Ricoult, K. Adib, T.S. Clair, B. Luerssen, L. Gregoratti, A. Barinov, 16th International Conference on Solid State Ionics, Shanghai, China, July 01–06 2007.